Investigation of gear rattle noise including visualization of vibro-impact regimes

Emmanuel Rigaud, Joël Perret-Liaudet

Investigation of gear rattle noise including visualization of vibro-impact regimes

Emmanuel Rigaud, Joël Perret-Liaudet

Laboratoire de Tribologie et Dynamique des Systèmes LTDS UMR5513

Université de Lyon, Ecole Centrale de Lyon, ENISE, ENTPE, CNRS

36 avenue Guy de Collongue, F-69134, ECULLY, France

Corresponding author: emmanuel.rigaud@ec-lyon.fr

Tel: +33 4 72 18 62 96

29 pages

1 table

13 figures

Abstract

This paper presents an experimental study of gear rattle noise induced by vibroimpacts between gear teeth. A specific device is designed to analyse the nonlinear dynamic behaviour of a spur gear submitted to input velocity fluctuation. After adjustment of the drag torque applied to the output gear and the operating backlash, the drive gear mean rotation speed, the velocity fluctuation amplitude and frequency are controlled during experiment. The dynamic transmission error is measured thanks to high resolution optical encoders. The originality of the device consists on a high-speed camera implemented in order to visualize the contact zone and to identify the occurrence of successive impacts between gear teeth. The rattle threshold is identified as a function of velocity fluctuation amplitude and frequency for various operating drag torques and mean rotation speeds. Experiments show a very good agreement with the theoretical master curve. Once impacts occur, stationary nonlinear gear dynamic response and rattle noise radiated by the mechanical system are investigated. Most of times, almost $1T$ periodic response with 2 impacts per period are observed, one impact between active flanks succeeding to one impact between reverse flanks. A contact phase between gear teeth is observed after each impact rather than an instantaneous rebound. Dynamic response frequency is independent of the mean rotation speed, so that several successive tooth pairs can cross the meshing zone without any contact between gear teeth. Analytical and numerical simulations performed using a gear rattle model show a good agreement with experiments. Finally, sound pressure emitted from the gear pair is measured and discussed in the light of energy transferred per second to the system during the successive impacts.

Keywords

Nonlinear dynamics, gear rattle, contact loss, impacts, dynamic transmission error, backlash, gear noise.

1 Introduction

Many mechanical-geared systems are subjected to such external excitations that some contact losses between gear teeth may occur, leading to rattle noise. The nonlinear gear dynamic response is then characterized by impacts between active and reverse tooth flanks. As a first example, roots vacuum pump presents this kind of behaviour. It is designed with two shafts supporting a pair of pumping lobes at each stage of the pump. The counter rotary motion of shafts is provided by an electric motor associated with a reverse gear (i.e. gear ratio equal to 1). When the limit pressure is reached, the mean drag torque and the contact mesh force are low. Consequently, contact losses between gear teeth may occur due to the fluctuations of the input torque and the fluid forces during the operating of the pump [1-3]. Another example corresponds to conventional manual automotive gearbox, for which the output gears of unselected ratios are subjected to a low drag torque. So, the engine torque fluctuation generates a velocity fluctuation of the drive gear leading to contact losses [4-12]. In both cases, the nonlinear dynamic behaviour of the output gears is characterized by impacts between active and/or reverse flanks leading to a broadband rattle noise emitted from the mechanical system.

More generally, the key parameters governing the nonlinear gear rattle dynamics are the velocity fluctuation of the drive gear, the inertia of the output gear, the low drag torque, the gear backlash and the elastic and damping characteristics during impacts [13]. Many investigations deal with the torsional analysis of the driveline dynamic behaviour in order to reduce velocity fluctuation of the drive gear [4-9]. Some other works deal with a 1 degree of freedom modelling of the gear pair including backlash non linearity. Nonlinear dynamic response induced by harmonic [14, 15], periodic [10, 16] or random excitation [17] has been studied. Effect of tooth profile errors and gear eccentricities which modify gear backlash amplitude and generate a secondary internal excitation source have also been analysed [18-20].

This paper presents an experimental study of the nonlinear dynamic behaviour of a spur gear. The aim is to identify gear rattle threshold and to characterize impact regimes for various operating conditions, and to compare results with those obtained from analytical and numerical models. The first part presents the

experimental device as well as the studied spur gear characteristics. The second part presents preliminary measurements of drag torque, operating gear backlash and static transmission errors generated by the contacts between active and reverse flanks. The third part compares the rattle threshold measurements to the corresponding analytical results. The fourth part investigates the nonlinear gear dynamic responses observed beyond the threshold for various operating conditions. Then, results are compared with analytical and numerical investigations. Finally, the rattle noise is measured and discussed in the light of impulses associated with the successive impacts.

2 Experimental set-up and instrumentation

The principle of the rattle experiments consists of generating and measuring the nonlinear dynamic behaviour of a reverse spur gear with a controlled operating backlash. Experiments are performed using the specific apparatus named LUG designed and built at the Tribology and System Dynamics Laboratory (LTDS) [21]. It is composed of a fixed aluminium plate attached to a concrete bloc supported by 4 air springs. The high mass (600 kg) of the whole bench leads to very low resonant frequencies decoupled from the gear rattle dynamics. A high precision spindle is located at the centre of the top plate. Its rotation is accurately controlled with a brushless synchronous motor allowing rotational speed Ω from 0 to 2000 rpm. The piloting of the test bench allows control of the mean rotation speed Ω_0, the velocity fluctuation amplitude $\Delta\Omega$ and frequency ω which can be adjusted independently of the mean rotation speed. The instantaneous velocity is then:

$$\Omega(t) = \Omega_0 + \Delta\Omega \sin(\omega t) \quad (1)$$

The piloting also allows some increasing and decreasing sweeps of parameters Ω_0, $\Delta\Omega$ and ω, one after the other, or simultaneously.

A specific module corresponding to a reverse spur gear has been assembled on the top plate (see figure 1). The rotation of the spindle generates the motion of the drive gear. This one meshes with an identical output gear (gear ratio: 1) supported by a ball bearings set-up. Gear characteristics are presented in

Table 1. As described in section 3, the center distance can be adjusted, leading to variations in contact ratio and operating backlash.

Number of teeth (Z_1=Z_2)	90
Normal module m_o	3.5 mm
Pressure angle α_0	20°
Tooth addendum coefficient	1
Tooth dedendum coefficient	1.25
Shift radius coefficient	0
Face width	7.5 mm
Centre distance a	315 to 318 mm
Operating backlash	0 to 2 mm
Contact ratio ε_a	1.84 to 1.02

Table 1: Spur gear characteristics.

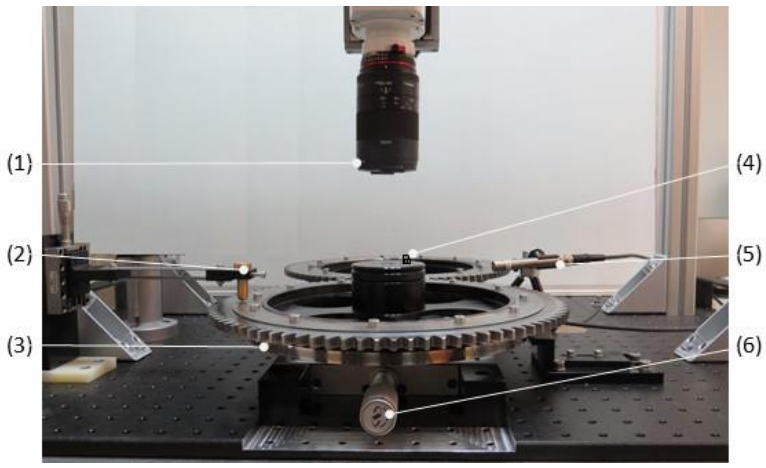

Figure 1: Experimental set-up. (1) High speed camera, (2) pin for additional drag torque, (3) optical encoder, (4) accelerometer, (5) microphone, (6) micrometric translation stage for adjustment of centre distance.

Angular displacements of gears θ_1 and θ_2 are measured thanks to the high resolution optical encoders (400 000 ppr). Acoustic response is measured thanks to a ½ in. microphone placed in the near-field, close to the gear meshing zone. Signals are acquired using a dynamic acquisition card with a high sampling

rate (50 kHz). The dynamic response of the gear and the impacts are also visualized thanks to a compact monochrome 1-megapixels high speed camera (Phantom Miro M310) with 3.2 Giga-pixels/second providing 3200 fps at maximum resolution (1280x800) and 12800 fps at resolution (640x400). The camera is coupled with direct and reverse lighting devices. Its sensor high light sensitivity and minimum exposure time (1 µs) offer high dynamic range and excellent image quality.

3 Drag torque, backlash and transmission error measurement

A residual drag torque T_r applied to the output gear is induced by the dissipation in the rolling element bearings. It is measured from the analysis of the free damped dynamic response of the output gear alone. For this, an initial rotation speed is introduced. The free damped angular motion of the output gear is measured thanks to the optical encoder, until motion stops. It shows a constant deceleration. Consequently, the corresponding residual drag torque is independent of angular velocity. The measured constant value is $T_r = 0.22$ N m. An additional drag torque T_a can be added by introducing a friction force through a sliding contact between the lateral surface of the output gear and a bronze pin subjected to a normal load (see figure 1). Measurement of deceleration of the output gear for successive normal loads applied to the sliding contact allows identification of the additional drag torque T_a which turns out to be independent of angular velocity. The range explored for the total drag torque T_d during the experimental campaign is $0.22 \leq T_d \leq 0.750$ N m.

The operating backlash amplitude associated with circumferential clearance between active and reverse flanks can be adjusted by changing the centre distance thanks to a micrometric translation stage supporting the output gear. The range explored for the operating backlash during the experimental campaign is $0 \leq b \leq 2$ mm.

The transmission error (TE) is defined as the difference between the actual position of the output gear and the position it would occupy if the gear drive were perfect [22]. TE along the line of action is equal to $R_b(\theta_1 - \theta_2)$ where R_b is the base radius for both wheels and θ_1, θ_2 are respectively the input and the

output gear angular positions. For a very low rotation speed and a very low applied load such as the gear teeth deflection is negligible, the unloaded static transmission error (STE) results from tooth flank corrections and gear manufacturing errors. Under other operating conditions, the dynamic transmission error (DTE) corresponds to the gear dynamic response to the different excitation sources. STE between active flanks, referred as $R_b\varphi(\theta_1)$, STE between reverse flanks, referred as $R_b\psi(\theta_1)$, and the operating backlash $R_b(\varphi - \psi)$ can be measured thanks to a single experiment. For this, a very low counter clockwise motion of the drive gear ($\Omega_0 = +1$ rpm) is introduced and allows measurement of STE between the active flanks. Once the angular distance corresponding to a fundamental period is travelled (360° for a reverse gear), the rotation speed is reversed ($\Omega_0 = -1$ rpm). The clockwise motion allows measurement of STE between the reverse flanks. The gap between the two curves corresponds to the gear backlash amplitude.

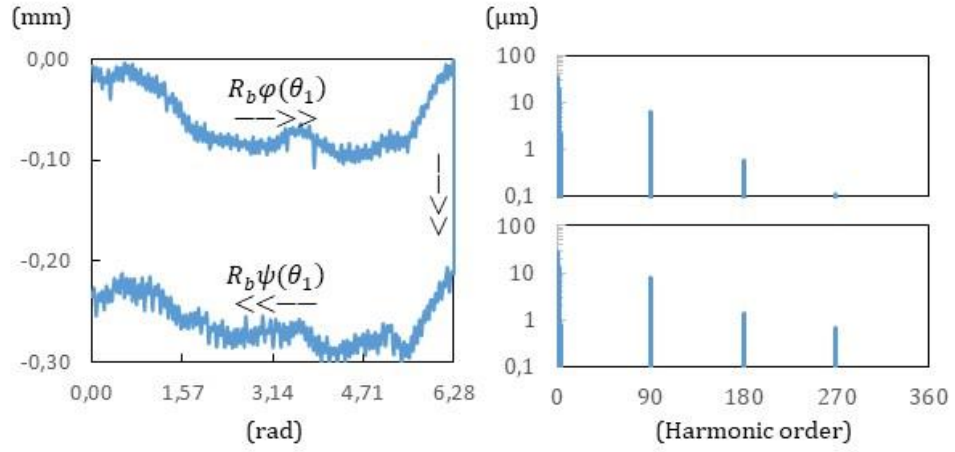

Figure 2: Unloaded static transmission errors generated by contact between active and reverse flanks.

Figure 2 displays the time evolution and the amplitude spectra of both unloaded STE. Time fluctuation firstly shows low frequency components (harmonics H_1, H_2, H_3 of the fundamental period 360°) related to wheel shape defects and mounting errors such as eccentricities. Its peak-to-peak amplitude during a rotation period is equal to 100 µm. STE fluctuation secondly shows mesh frequency components (H_{90}, H_{180}, etc.) related to the tooth profile errors. Its peak-to-peak amplitude during a mesh period is equal to

10 µm. For this experiment and the centre distance chosen, the backlash amplitude is almost constant and is equal to 250 µm.

4 Measurement of rattle threshold

The first step of the experimental campaign consists of measuring the rattle threshold beyond which impacts occur. Experiments are performed different sets of drag torque T_d, mean rotation speed Ω_0 and velocity fluctuation amplitude $\Delta\Omega$. For each operating condition, a slow increasing sweep of the excitation frequency ω is performed until rattle arises. Then, a slow decreasing sweep of the excitation frequency ω is performed until rattle collapses. The frequency ω_c for the collapsing threshold is observed to be lower than or equal to the frequency ω_a for the arising threshold. Nevertheless, the values of ω_a and ω_c are very close whatever the operating conditions.

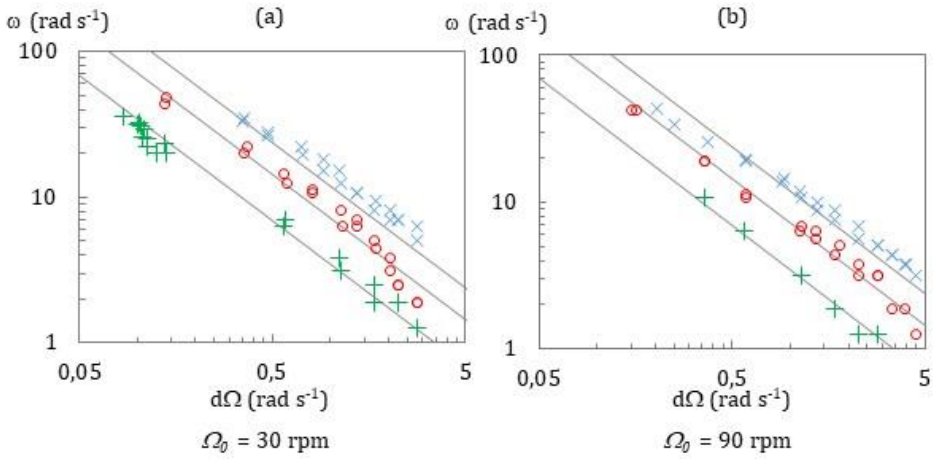

Figure 3: Experimental rattle threshold. Drag torque $T_d = 0.22$ N m (++++++), $T_d = 0.46$ N m (°°°°°°°°), $T_d = 0.75$ N m (xxxxxx).

Figure 3 displays results obtained for the arising rattle threshold in the log-log scale plane $(\Delta\Omega, \omega)$, for three drag torques ($T_d = 0.22$, 0.46 and 0.75 N m), two mean rotation speeds ($\Omega_0 = 30$ rpm, figure 3a and 90 rpm, figure 3b) and a large set of velocity fluctuations $\Delta\Omega$ in-between 0.5 and 50 rpm corresponding to the range $[0.05 - 5\, r\text{ad s}^{-1}]$. For each drag torque value, the curve describing the

logarithm of the velocity fluctuation frequency vs velocity fluctuation amplitude shows a linear decreasing with a slope close to (-1). Comparison between figures 3a and 3b confirms that the experimental rattle threshold does not depend of the mean rotation speed Ω_0.

From a theoretical point of view, teeth contact loss occurs when the acceleration $\ddot{\theta}_2$ of the output gear (whose inertia is noted J) imposed by the drive gear motion θ_1 becomes such the inertial torque $J\ddot{\theta}_2$ exceeds the drag torque T_d [12]. Therefore, the rattle threshold is given by the following condition:

$$\max\left(\ddot{\theta}_2\right) = T_d/J \tag{2}$$

For an applied load such as the gear teeth deflection is negligible and contact between gear teeth, the forced angular position of the output gear θ_2 is related to the input angular position θ_1:

$$\theta_2 = \theta_1 + \varphi(\theta_1) \tag{3}$$

where $\varphi(\theta_1)$ corresponds to the unloaded STE. Consequently, angular velocity and acceleration of the output gear during contact are given by:

$$\ddot{\theta}_2 = \ddot{\theta}_1 + \varphi'(\theta_1)\ddot{\theta}_1 + \varphi''(\theta_1)\dot{\theta}_1^2 \tag{4}$$

where the prime sign corresponds to the derivative with respect to θ_1. In order to analyse rattle gear phenomena and threshold, a harmonically varying input velocity is introduced (see equation (1), section 2). Consequently, the drive gear angular acceleration is:

$$\ddot{\theta}_1 = \omega\Delta\Omega\cos(\omega t) \tag{5}$$

Finally, the rattle threshold is governed by the following condition:

$$\max\left(\ddot{\theta}_1 + \varphi'(\theta_1)\ddot{\theta}_1 + \varphi''(\theta_1)\dot{\theta}_1^2\right) = T_d/J \tag{6}$$

The objective of experiments performed is to generate the gear teeth contact losses and to control the impacts threshold from the drive gear velocity fluctuation and not from the static error. For this, the experimental values of parameters Ω_0, $\Delta\Omega$, and ω have been chosen in order to remain the additional terms $\varphi'(\theta_1)\ddot{\theta}_1$ and $\varphi''(\theta_1)\dot{\theta}_1^2$ negligible compared to the maximum value of the direct forcing acceleration term $\ddot{\theta}_1$. Therefore, the rattle threshold criterion can be written as follows:

$$\omega\,\Delta\Omega = \max\left(\ddot{\theta}_1\right) \approx \max\left(\ddot{\theta}_2\right) = T_d/J \tag{7}$$

The ratio between the acceleration force of the driving gear and the drag force allows introduction of the dimensionless excitation level [12]:

$$\Lambda = J\,\omega\,\Delta\Omega/T_d \tag{8}$$

The rattle threshold criterion Λ^* is:

$$\Lambda^* = 1 \tag{9}$$

Corresponding to:

$$\log\omega = -\log\Delta\Omega/T_d - \log J \tag{10}$$

Figure 4 displays the theoretical rattle threshold master curve in the log-log scale plane ($\Delta\Omega/T_d$, ω). The slope is equal to (-1) in accordance with equation (10). Figure 4 shows that rescaling of the experimental data leads to a very good agreement with the theoretical master curve, whatever the applied drag torque. The set of measurements carried out corresponds to a mean value of the dimensionless excitation level $\Lambda^*_{exp} = 1.09$ (standard deviation 0.19).

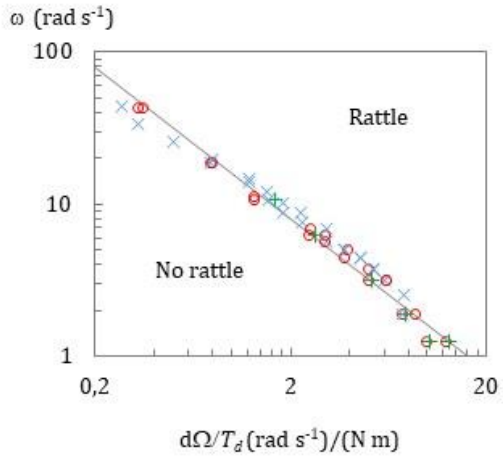

Figure 4: Theoretical rattle threshold master curve (black line) and rescaled experimental data. Drag torque $T_d = 0.22$ N m (++++++), $T_d = 0.46$ N m (°°°°°°°°), $T_d = 0.75$ N m (xxxxxx).

5 Nonlinear gear dynamic responses under stationary conditions

The next step of the experimental campaign consists of measuring the impact response beyond the rattle threshold, in order to characterize the corresponding gear nonlinear dynamic behaviour.

First, the effect of velocity fluctuation amplitude $\Delta\Omega$ is analysed for a chosen excitation frequency ω. Figure 5 displays the gear dynamic responses for increasing velocity fluctuation amplitudes $\Delta\Omega = 0, 1.6, 5$ and 20 rpm, corresponding to a velocity fluctuation along the line of action up to 310 mm s^{-1}. The mean operating speed is $\Omega_0 = 30$ rpm, the drag torque is $T_d = 0.22$ N m and the excitation frequency is $\omega/2\pi = 3$ Hz.

The first column displays the time evolutions of the displacement dynamic transmission error $R_b(\theta_2 - \theta_1)$. The up and down frontiers correspond to transmission errors between active flanks $R_b\varphi(\theta_1)$ and reverse flanks $R_b\psi(\theta_1)$. Successive contact losses can be easily observed. The second column displays the time derivative of the dynamic transmission error, defined by the relative velocity $R_b(\dot{\theta}_2 - \dot{\theta}_1)$. Positive peaks correspond to impacts between active flanks and negative peaks correspond to impacts between reverse flanks. Considering at what time successive impacts occur, the third column displays the Poincaré sections corresponding to the impact velocity versus the phase relative to the excitation frequency. The successive responses allow analysis of the velocity fluctuation influence. For a very low amplitude ($\Delta\Omega \approx 0$ rpm), an almost permanent contact between the active flanks is observed, even if the displacement response shows few peaks revealing light contact losses. Consequently, the dynamic transmission error $R_b(\theta_2 - \theta_1)$ is similar to the static transmission error $\varphi(\theta_1)$ displayed in figure 2. When the velocity fluctuation is increased ($\Delta\Omega = 1.6$ rpm), the rattle threshold is reached. The nonlinear dynamic response shows noticeable contact losses and impacts. The excitation amplitude is still too low to cross the gear backlash. Consequently, impacts only occur between active flanks with a low impacting velocity. For $\Delta\Omega \geq 5$ rpm, the excitation amplitude leads to succeeding impacts between active and reverse flanks. The displacement responses show that the output gear crosses the gear backlash forward and backward. Each impact is followed by a persistent contact period between the gear teeth. The free

flight period and the following persistent contact period show a duration of the same order of magnitude. Considering the period of the excitation $T = 2\pi/\omega$, the gear dynamics corresponds to a $1T$ periodic response with 2 impacts per period. Poincaré sections show that impact phases and impacting velocities are almost constant for all the successive impacts between active flanks, as well as for all the impacts between reverse flanks.

Second, the effect of the excitation frequency ω is analysed for a chosen velocity fluctuation amplitude $\Delta\Omega$. Figure 6 displays the gear dynamic response for increasing velocity fluctuation frequencies $\omega/2\pi = 1,\ 3,\ 5$ and 10 Hz. The mean operating speed is $\Omega_0 = 30$ rpm, the drag torque is $T_d = 0.22$ N m and the velocity fluctuation amplitude is $\Delta\Omega = 5$ rpm. The successive responses allow analysis of the excitation frequency influence and leads to similar conclusions. For a very low frequency $\omega/2\pi < 1$ Hz, a permanent contact between the active flanks is observed. For $\omega/2\pi = 1$ Hz, the rattle threshold is reached. Some bursts of light impacts between active flanks occur. For $\omega/2\pi = 3,\ 5$ and 10 Hz, the dynamic $1T$ periodic responses previously identified are observed. The dates of successive impacts are only related to the excitation frequency which is much lower than the mesh frequency. Consequently, several successive tooth pairs may cross the meshing zone without any contact between gear teeth.

Each Poincaré section displayed in figures 5 and 6 shows that the impacting velocity between active flanks is slightly higher than that between reverse flanks (for example, for $\Delta\Omega = 20$ rpm and $\omega/2\pi = 3$ Hz, mean values of impacting velocities are $22.3\ \text{mm s}^{-1}$ and $-19.9\ \text{mm s}^{-1}$. Standard deviation is $2.1\ \text{mm s}^{-1}$). Successive Poincaré sections obviously show that the impacting velocity is governed by the velocity fluctuation amplitude and frequency. Figure 7 displays the evolution of the mean value of the squared impacting velocity (proportional to the kinetic energy) versus the product between the velocity fluctuation amplitude and the velocity fluctuation frequency ($\omega.\Delta\Omega$) for various operating conditions. Vertical bars correspond to standard deviation measured for all the impacts during the experiment. For convenient reasons, a log-log scale is chosen. The slope is equal to $(+10\ \text{dB/decade})$,

showing a linear relationship between the impacting kinetic energy and the product $(\omega.\Delta\Omega)$. Moreover, a slight difference between the active and reverse flanks impacting velocity is confirmed.

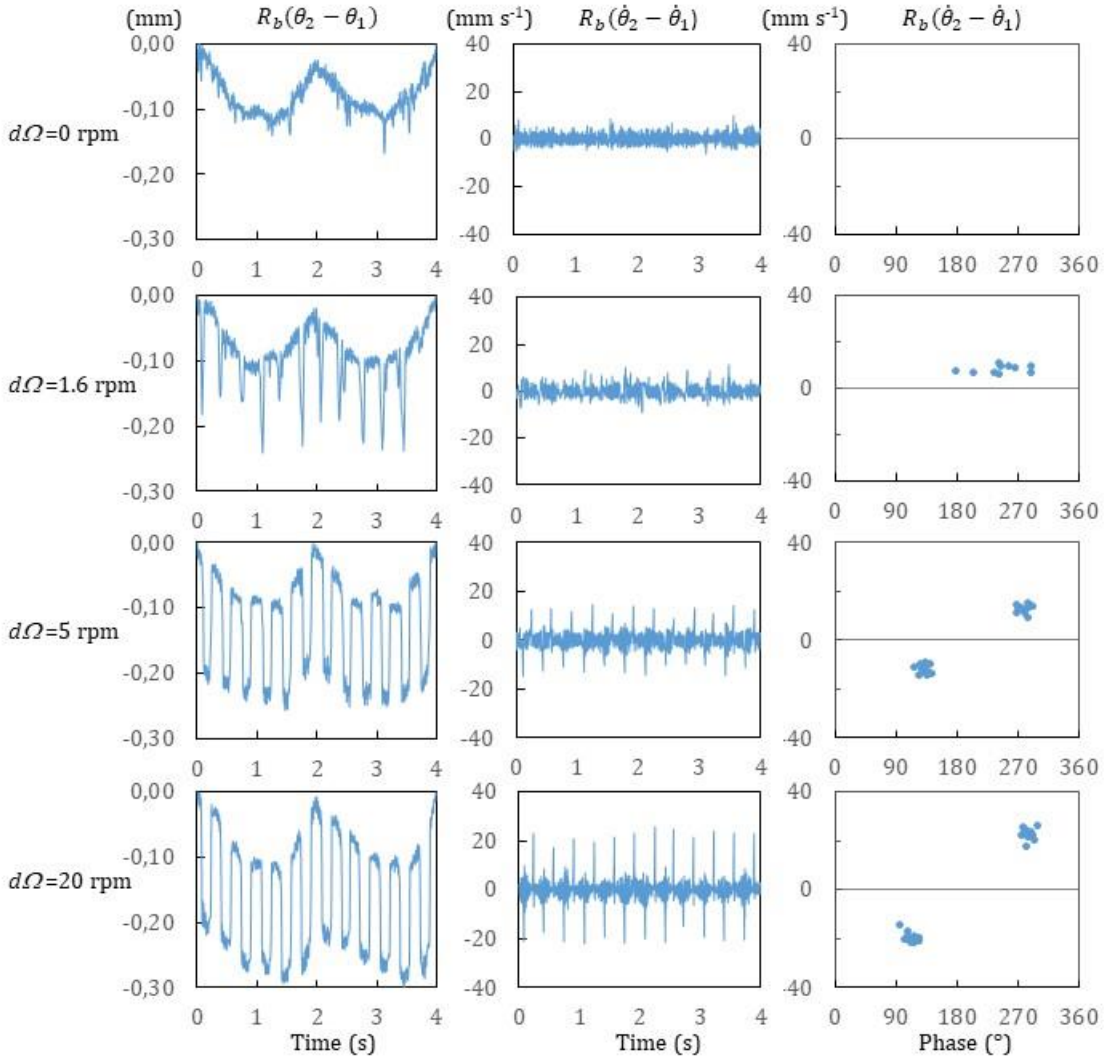

Figure 5: Impact response for increasing amplitude of velocity fluctuation $\Delta\Omega$. ($\Delta\Omega = 0, 1.6, 5$ and 20 rpm). $\Omega_0 = 30$ rpm, $\omega/2\pi = 3$ Hz, $T_d = 0.22$ N m. Column 1: dynamic transmission error $R_b(\theta_2 - \theta_1)$, column 2: velocity dynamic transmission error $R_b(\dot{\theta}_2 - \dot{\theta}_1)$, column 3: Poincaré sections - impacting velocity vs. phase.

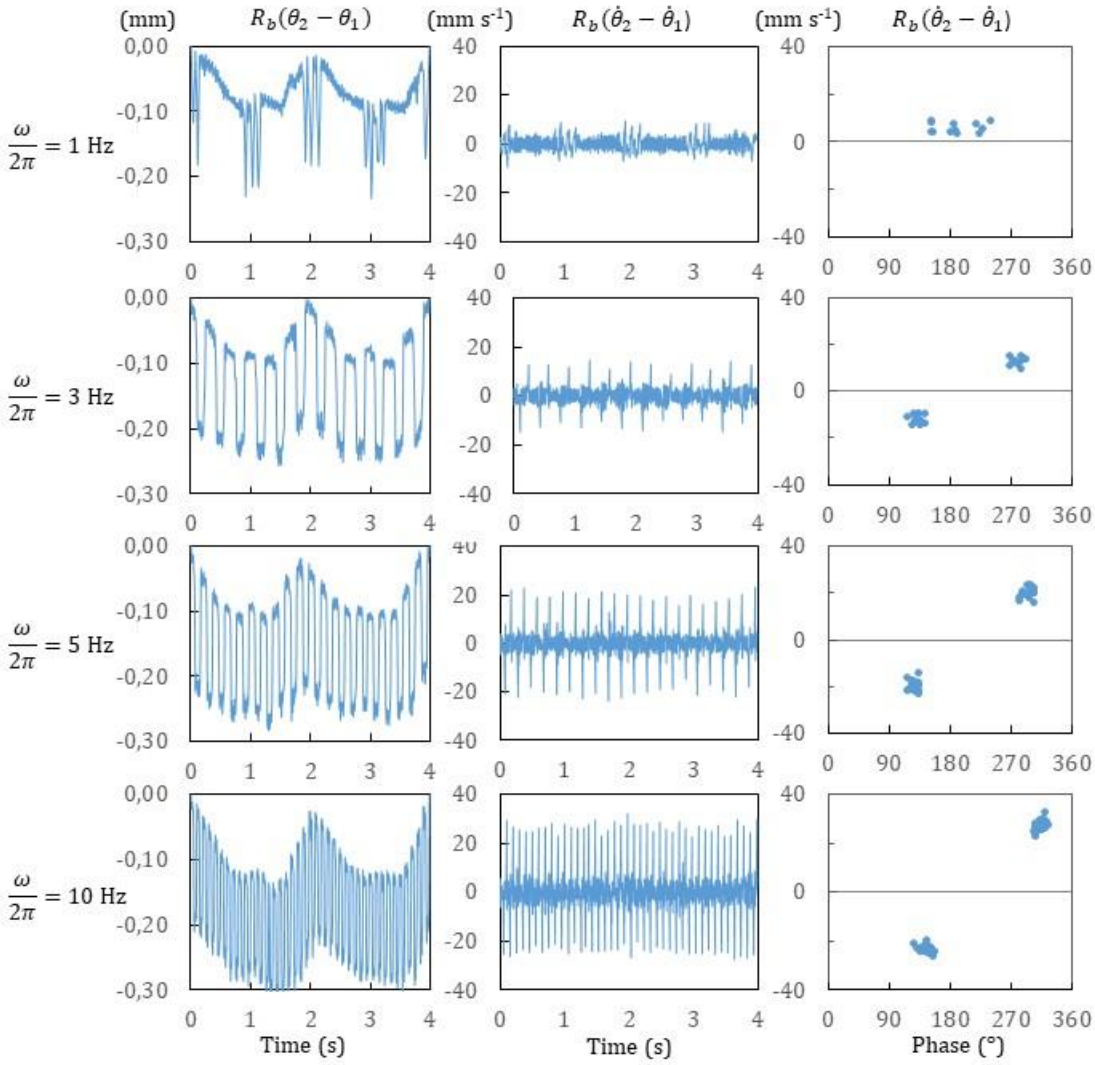

Figure 6: Impact response for increasing amplitude of excitation frequency ω ($\omega/2\pi = 1, 3$ 5 and 10 Hz). $\Omega_0 = 30$ rpm, $\Delta\Omega = 5$ rpm, $T_d = 0.22$ N m. Column 1: dynamic transmission error $R_b(\theta_2 - \theta_1)$, column 2: velocity dynamic transmission error $R_b(\dot{\theta}_2 - \dot{\theta}_1)$, column 3: Poincaré sections - impacting velocity vs. phase.

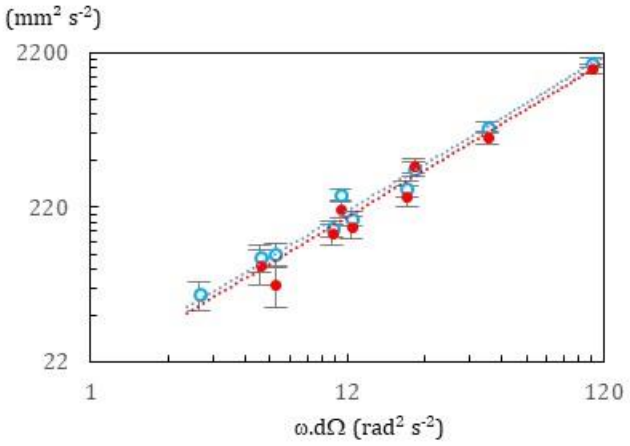

Figure 7: Mean value and standard deviation of the squared impacting velocity $v_{\perp}^2$ versus $(\omega.\Delta\Omega)$. Impacts between active flanks (o). Impacts between reverse flanks (•). $\Omega_0 = 30$ rpm, $T_d = 0.22$ N m.

The visualization of the contact zone with a high speed camera confirms the nonlinear behaviour induced by contact losses and the measurements performed in stationary conditions. The video post-processing allows measurement of the instantaneous position of the gears from the shape recognition. The visualization of the contact zone confirms at what time the impacts between active and reverse flanks occur. It also allows measurement of the contact and free flight motion durations, as well as the impacting velocity. Figure 8 displays a sequence of images of the contact along a period of excitation. The mean rotation speed is $\Omega_0 = 90$ rpm. The velocity fluctuation amplitude is $\Delta\Omega = 5$ rpm and its frequency is $\omega/2\pi = 3$ Hz . The excitation period is then $T = 0.333$ ms. The drive gear is on the right side and its motion is counter clockwise. First, contact between active flanks is observed ($t = 0$, tooth pair N°1, and $t = T/8$ tooth pairs N°6-7). Then, contact loss occurs and the output gear shows a free flight motion ($t = T/4$, tooth pair N°12, and $t = 3T/8$, tooth pair N°18) until contact between reverse flanks occurs ($t = T/2$, tooth pair N°24, and $t = 5T/8$, tooth pairs N°29-30). Contact loss occurs again and the output gear shows a reverse free flight motion ($t = 3T/4$, tooth pair N°35, and $t = 7/8$, tooth pairs N°40-41) until contact between active flank occurs ($t = T$, tooth pair N°46). The free flight duration and the contact duration are much longer than the meshing period. Consequently, visualization confirms that several

successive tooth pairs are in contact and several successive tooth pairs can cross the meshing zone without any contact between gear teeth.

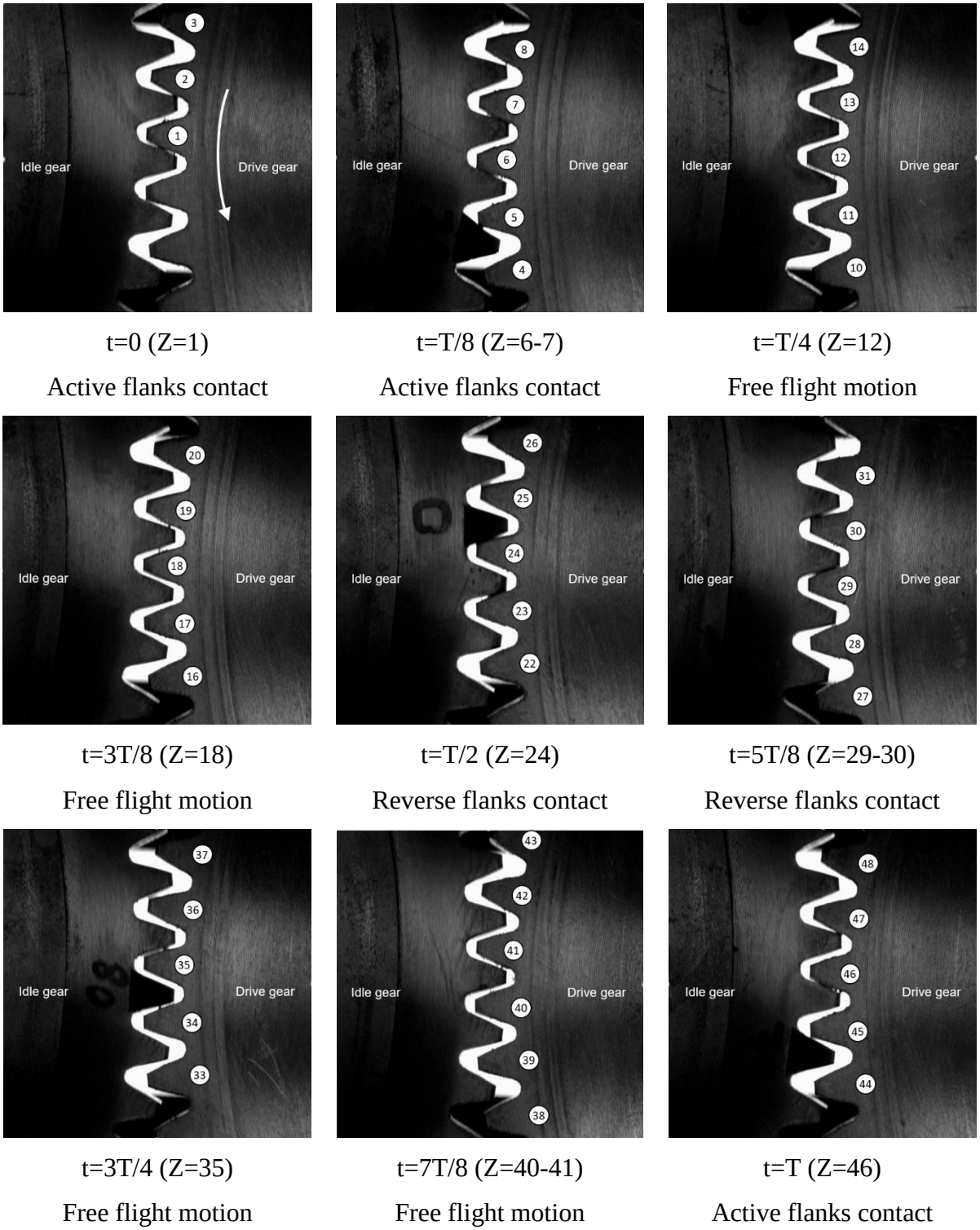

t=0 (Z=1) Active flanks contact

t=T/8 (Z=6-7) Active flanks contact

t=T/4 (Z=12) Free flight motion

t=3T/8 (Z=18) Free flight motion

t=T/2 (Z=24) Reverse flanks contact

t=5T/8 (Z=29-30) Reverse flanks contact

t=3T/4 (Z=35) Free flight motion

t=7T/8 (Z=40-41) Free flight motion

t=T (Z=46) Active flanks contact

Figure 8: Visualization of the contact with a high speed camera ($\Omega_0 = 90$ rpm, $\Delta\Omega = 5$ rpm, $\omega/2\pi = 3$ Hz, $T = 0.333$ ms).

6 Theoretical results

6.1 The mathematical model

As shown in previous works, the bouncing ball model with two moving walls excited by the velocity fluctuation suits to describe gear rattle dynamics [12]. Figure 9 displays the corresponding dynamic model.

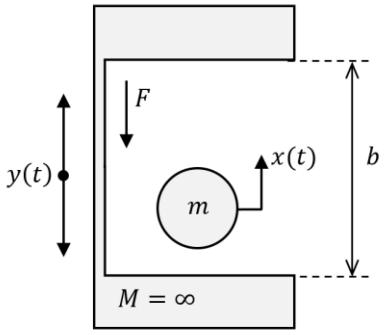

Figure 9: The dynamic model.

$x(t) = R_b\theta_2(t)$ and $y(t) = R_b\theta_1(t)$ are the output gear and drive gear displacements along the line of action. $(x - y) = R_b[\theta_2(t) - \theta_1(t)]$ is the transmission error (TE). Gear backlash amplitude b is assumed to be constant. $F = T_d/R_b$ is the drag force. $m = J/R_b^2$ is an equivalent mass assigned to the output gear. The drive gear motion is imposed and its mass is assumed infinite. Considering a purely harmonic fluctuation of the drive gear velocity $\dot{y}(t)$ along the line of action (see equation (1)) leads to:

$$\dot{y}(t) = R_b(\Omega_0 + \Delta\Omega \sin\omega t) = V_0 + \Delta V \sin\omega t \tag{11}$$

The same dynamic behavior is observed in the frame uniformly translated at speed V_0, such that equation (11) can be replaced by:

$$\dot{y}(t) = R_b\Delta\Omega \sin\omega t = \Delta V \sin\omega t \tag{12}$$

The displacement and acceleration of the drive gear in this moving frame are:

$$y(t) = -\frac{\Delta V}{\omega}\cos\omega t \tag{13}$$

$$\ddot{y}(t) = \omega\Delta V \cos\omega t \tag{14}$$

The free flight motion of the output gear initiated at time t_i is deduced from the equation of motion $m\ddot{x} = -F$ and is written as follows:

$$x(t) = -\frac{F}{2m}(t - t_i)^2 + \dot{x}_i(t - t_i) + x_i \quad (15)$$

with $$\dot{x}_i = \Delta V \sin \omega t_i$$

The output gear response is $x_i = -\Delta V/\omega \cos \omega t_i$ when it loses contact between active flanks and $x_i = b - \Delta V/\omega \cos \omega t_i$ when it loses contact between reverse flanks. Equation (15) remains valid as long as $y < x < y + b$. First, instantaneous impacts are assumed between active ($x = y$) and reverse flanks ($x = y + b$). The change in relative velocity between drive and output gears just after and before the impact is calculated from the usual relation:

$$\dot{x}_{i+} - \dot{y}_i = -e(\dot{x}_{i-} - \dot{y}_i) \quad (16)$$

$\dot{x}_{i-}$ is the absolute impacting velocity of the output gear at the i^{th} impact. $\dot{x}_{i+}$ is the rebound velocity of the output gear. $\dot{y}_i$ is the velocity of the drive gear. e is the coefficient of restitution ($0 \leq e \leq 1$).

Dates of successive impacts are identified by solving collision conditions in order to simulate the dynamic response. an alternative solution consists of integrating equation of motion, which requires introduction of Lagrange multiplier with Signorini condition, or penalty stiffness assuming very short impact duration. Both approaches have been performed.

6.2 The perfectly plastic case ($e = 0$)

Experiments show that a quasi-persistent contact between drive and output gears occurs after each impact. A simple way to model this behaviour is to consider perfectly plastic impact with $e = 0$. The persistent contact is observed until the imposed acceleration reaches the drag force, just like for the rattle threshold condition. Dates of successive contact losses between active and reverse flanks can thus be identified. The dynamic response is periodic at the excitation frequency, in particular because the memory of the impacting velocity is lost. Equations modelling the problem can be summarized as follows. The date t_1 for which contact loss between active flanks occurs is such that:

$$m\omega\Delta V \cos \omega t_1 = F \quad (17)$$

with $0 < \omega t_1 < \pi/2$

The date t_2 impact occurs between reverse flanks is such that:

$$\frac{F}{2m}(t_2 - t_1)^2 - \Delta V(t_2 - t_1)\sin \omega t_1 - \frac{\Delta V}{\omega}(\cos \omega t_2 - \cos \omega t_1) + b = 0 \quad (18)$$

The date t_3 for which contact loss between active flanks occurs is such that:

$$m\omega\Delta V \cos \omega t_3 = F \quad (18)$$

with $\pi/2 < \omega t_3 < \pi$

The date t_4 for which impact occurs between reverse flanks is such that:

$$\frac{F}{2m}(t_4 - t_3)^2 - \Delta V(t_4 - t_3)\sin \omega t_3 - \frac{\Delta V}{\omega}(\cos \omega t_4 - \cos \omega t_3) - b = 0 \quad (19)$$

Finally, the response is T-periodic with $T = 2\pi/\omega$.

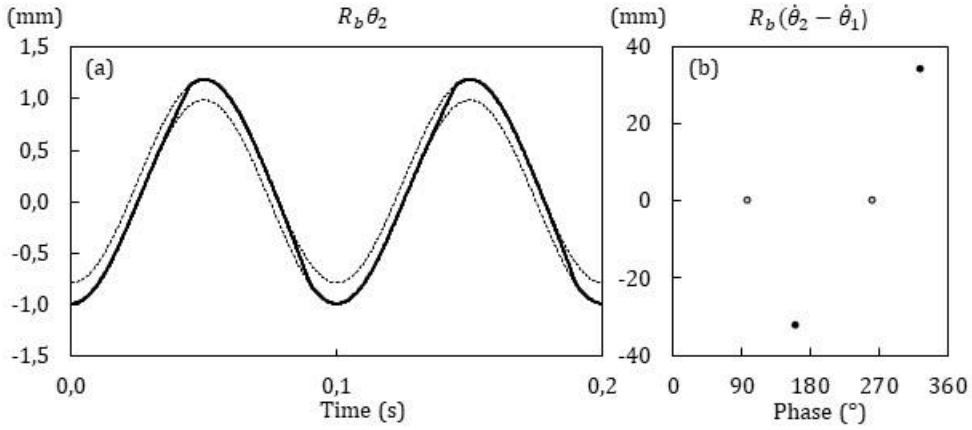

Figure 10: The dynamic displacement response (a) and its associated Poincaré section (b). Dashed line: active and reverse flanks of the drive gear displacements. Solid line: output gear displacement. Black points: impacts. grey points: contact losses. $b = 200$ µm, $T_d = 0.22$ N m, $\Delta\Omega = 4$ rpm, $\omega/2\pi =$ 10 Hz and $e = 0$.

Figure 10 displays the corresponding dynamic response. Operating conditions are backlash amplitude $b = 200$ µm, drag torque $T_d = 0.22$ N m, velocity fluctuation amplitude $\Delta\Omega = 4$ rpm and frequency

$\omega/2\pi =$ 10 Hz. Figure 10(a) displays the prescribed displacements of the active and the reverse flanks of the drive gear (dashed lines), and the dynamic response of the output gear (solid line). Figure 10(b) displays the Poincaré section corresponding to the relative impacting velocity versus the impact phases relative to the excitation frequency (black points). Figure 10(b) also displays contact loses dates with corresponding null relative velocity (grey points).

6.3 The inelastic case ($0 < e < 1$)

The perfectly plastic case ($e = 0$) may be physically inappropriate. Some simulations have been performed for a partially inelastic case by introducing penalty stiffness to take account of the contact conditions. Figure 11 shows that the persistent contact phase observed during the motion is observed. Operating conditions are backlash amplitude $b = 200$ µm, drag torque $T_d = 0.22$ N m, velocity fluctuation amplitude $\Delta\Omega = 4$ rpm and frequency $\omega/2\pi =$ 10 Hz. The coefficient of restitution is $e = 0.3$. Energy loss during contact has been introduced via an equivalent viscous damping coefficient during contact deduced from the coefficient of restitution e and given by [24, 25]:

$$\zeta = -\log e/\sqrt{\pi^2 + \log e} \tag{20}$$

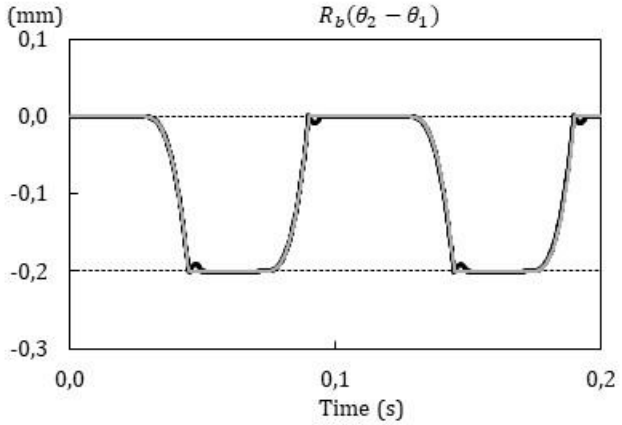

Figure 11: Relative dynamic response of the output gear in between the active and reverse flanks of the drive gear. Grey line: $e = 0$. Black line: $e = 0.3$. $b = 200$ µm, $T_d = 0.22$ N m, $\Delta\Omega = 4$ rpm and $\omega/2\pi =$ 10 Hz.

Next simulations have been performed taking account of the excitation source induced by the STE. As shown in figure 2, STE time fluctuation firstly shows components at the rotational frequency induced by wheel shape defects and eccentricities and secondly shows components at the mesh frequency induced by tooth profile errors. Therefore, two additional harmonic excitations have been superimposed to the external excitation, leading to:

$$y(t) = -\frac{\Delta V}{\omega}\cos\omega t + Y_1\cos(\Omega_0 t - \varphi_1) + Y_{90}\cos(90\Omega_0 t - \varphi_{90}) \quad (21)$$

Amplitudes Y_1, Y_{90} and phases φ_1, φ_{90} are adjusted according to the experimental data.

Figure 12 displays numerical dynamic responses for several operating conditions corresponding to experimental results observed in figures 5 and 6. Results correspond to a coefficient of restitution $e = 0.5$. A very good agreement between experimental and numerical results is observed. the proposed modelling and numerical time integration scheme are quite appropriate to describe the nonlinear gear dynamic response beyond the rattle threshold. In particular, the dynamic responses are very well predicted for operating conditions just beyond the rattle threshold (see the two first dynamic responses displayed in figure 12 and the corresponding dynamic responses displayed in figures 6a and 5b). Taking into account the static transmission error leads to slightly premature contact losses. Nevertheless, once the 1T periodic response with 2 impacts per period established, the influence of static transmission error is negligible for the chosen mean operating speed, compared to the influence of velocity fluctuation, even if it leads to a slight dispersion on the impacting velocity and phase.

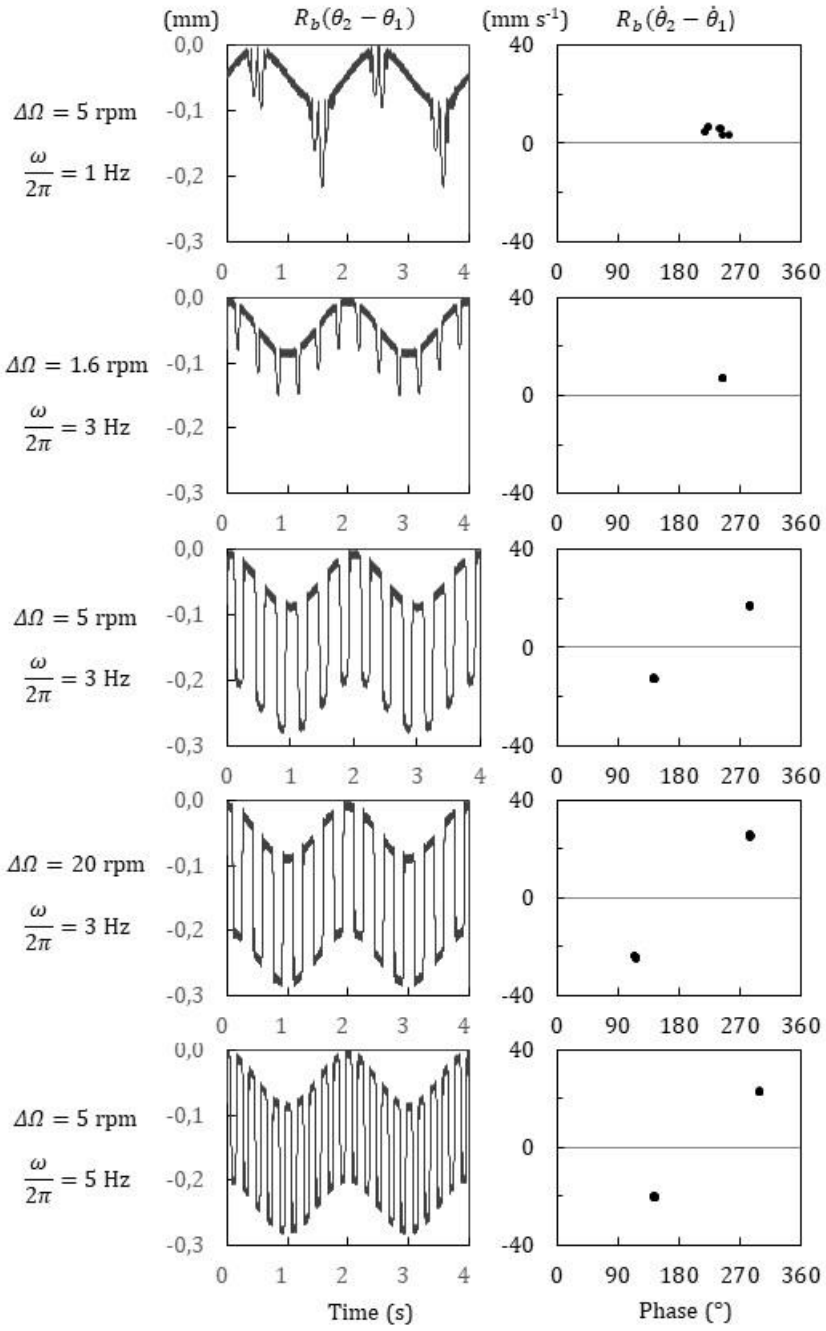

Figure 12: Relative dynamic response of the output gear in between the active and reverse flanks of the drive gear. Time history and Poincaré section. $e = 0.5, \Omega_0 = 30$ rpm, $T_d = 0.22$ N m.

7 Gear rattle noise induced by impacts

Below the rattle threshold, the noise radiated by the gear pair corresponds to the whining noise generated by the meshing process [26, 27]. For a mean operating speed $\Omega_0 = 30$ rpm and a residual drag torque $T_d = 0.22$ N m, the sound pressure measured thanks to the microphone in the near-field close to the gear meshing zone is equal to:

$$L_{p-w} = 78 \text{ dB} \tag{22}$$

with $$L_{p-w} = 10\ log\left(\frac{P}{P_{ref}}\right)^2 = 20\ log\left(\frac{P}{P_{ref}}\right)$$

and $$P_{ref} = 2\ 10^5 \text{ Pa}$$

Beyond the rattle threshold, an increase of the sound pressure with velocity fluctuation amplitude and frequency is observed. The purpose of this section is to establish the correlation between the sound pressure amplitude and the successive impacts. An almost linear increasing of the impacting kinetic energy E with the product between velocity fluctuation amplitude and frequency is observed in figure 7:

$$E \propto \omega.\Delta\Omega \tag{23}$$

A persistent contact rather than an instantaneous rebound is observed after the impact, so that the impacting kinetic energy is transferred to the system, because. Moreover, once the periodic 1T response is established with 2 impacts per period, the number of impacts n per second is proportional to the excitation frequency:

$$n = \omega/\pi \tag{24}$$

Let's assume the acoustic power generated by the successive impacts is proportional to the sum of energy transferred to the system per second:

$$\Pi_{ac} \propto \omega^2.\Delta\Omega \tag{25}$$

This leads to a rattle sound pressure generated by the successive impacts as follows:

$$L_{p-r} = 10\ log(A.\omega^2.\Delta\Omega) \tag{26}$$

Where A is constant and depends on parameters such as the equivalent impacting mass *m*, the radiating surface of the experimental system and the distance between the source and the microphone. The total sound pressure generated by both whining and rattle noises is:

$$L_p = 10\ log\left(10^{L_{p-w}/10} + 10^{L_{p-r}/10}\right) \quad (27)$$

Figure 13 displays the evolution of experimental sound pressure (dB) versus $(\omega^2.\Delta\Omega)$ for several velocity fluctuation amplitudes ($\Delta\Omega$ =1.6, 5, 10 and 20 rpm) and frequencies ($\omega/2\pi$ = 1, 2, 3, 5 and 10 Hz). 3 curves are added. The first one corresponds to the sound pressure amplitude L_{p-w} generated by the whining noise for the mean operating speed and measured below the rattle impact threshold (eq. (22)). The second one corresponds to the sound pressure amplitude L_{p-r} generated by the rattle noise and is deduced from the assumption that the acoustic power induced by the successive impacts is proportional to the sum of energy transferred to the system per second (eq. (26)). The last one corresponds the total sound pressure L_p which takes account of the coexistence of both whining and rattle noises (eq. (27)). The experimental measurements show a good agreement with eq. (27), whatever the velocity fluctuation amplitude and frequency. This confirms that the acoustic power induced by the rattle varies linearly with $(\omega^2.\Delta\Omega)$ and is related to the kinetic energy transferred to the system per second by the successive impacts. For low amplitudes of $(\omega^2.\Delta\Omega)$, the whining noise is much higher than the rattle noise, even if the successive impacts are clearly audible once they occur. For larger amplitudes of $(\omega^2.\Delta\Omega)$, the rattle noise induced by the successive impacts masks the whining noise.

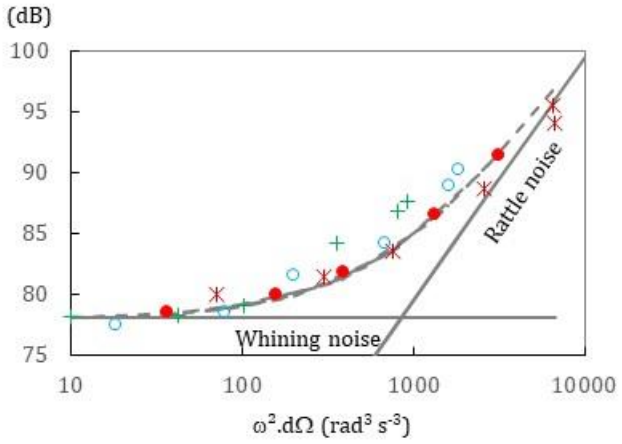

Figure 13: Evolution of the sound pressure L_p (dB) vs ($\omega^2.\Delta\Omega$).

($\omega/2\pi$ = 1, 2, 3, 5, 10 Hz) ($\Delta\Omega$ = 1.6 rpm (°°°), 5 rpm (+++), 10 rpm (•••), 20 rpm (***).

8 Conclusion

The experimental nonlinear rattle dynamic behaviour of a spur gear submitted to velocity fluctuation has been investigated using a specific device. After adjustment of drag torque and gear backlash, piloting of the device allows control of the mean rotational speed, the velocity fluctuation amplitude and its frequency. The dynamic transmission error is measured thanks to high resolution optical encoders. Results highlight contact losses and impacts between active and reverse flanks. Theoretical rattle threshold master curve is confirmed by experiments performed for various operating conditions. Arising and collapsing of contact losses are governed by the velocity fluctuation amplitude and frequency. They are independent of the gear mean rotation speed. In the range of operating speeds explored, the influence of static transmission error excitation source is also negligible.

Beyond the rattle threshold, nonlinear gear dynamic response is characterized for several mean rotation speeds, velocity fluctuation amplitudes and excitation frequencies. Most of time, an almost 1T periodic response with 2 impacts per period of excitation is observed, one impact between active flanks succeeding to one impact between reverse flanks. A contact phase between gear teeth is observed after each impact rather than an instantaneous rebound. The kinetic energy transferred to the system during the impact shows a linear variation with the product between velocity fluctuation frequency and

amplitude ($\omega.\Delta\Omega$). The visualization of the contact with a high speed camera confirms at what time the impacts between active and reverse flanks occur. It also allows measurement of the contact duration, the free flight motion duration and the impacting velocity. Occurrence of successive impacts is related to the excitation frequency which is much lower than the mesh frequency. Visualization confirms that several successive tooth pairs are in contact and several successive tooth pairs can cross the meshing zone without any contact between gear teeth.

Theoretical and numerical results have been performed from a gear rattle model. Excitation source considered is the velocity fluctuation and eventually includes the static transmission error. A good agreement is observed with experimental results, both for the rattle threshold and for the nature of nonlinear dynamic responses. The proposed modelling and numerical time integration scheme are relevant to describe the nonlinear gear dynamic response.

Finally, noise emitted from the system can be interpreted from simultaneous consideration of whining and rattle sources. Assuming that acoustic power generated by the rattle is proportional to the sum of kinetic energy transferred per second to the system by the successive impacts is relevant for describing the sound pressure measured during rattle experiments. For low amplitude of parameter ($\omega^2.\Delta\Omega$), the successive impacts are clearly audible once they occur, but the sound pressure radiated from the system is mainly due to the gear whining noise. For larger amplitude of parameter ($\omega^2.\Delta\Omega$), the rattle noise induced by the successive impacts becomes the main source of acoustic nuisance.

Acknowledgement

The authors are members of the LabCom LADAGE (LAboratoire de Dynamique des engrenAGEs), created by the LTDS and the Vibratec Company and operated by the French National Research Agency (ANR-14-LAB6-0003). They are also members of the Labex CeLyA of Université de Lyon (ANR-10-LABX-0060/ANR-11-IDEX-0007).

References

[1] Garambois P., Donnard G., Rigaud E., Perret-Liaudet J. Multiphysics coupling between periodic gear mesh excitation and input/output fluctuating torque: application to a roots vacuum pump. Journal of Sound and Vibration, 405, 158–174, 2017.

[2] Mason J., Homer M., Wilson RE. Mathematical models of gear rattle in Roots blower vacuum pumps. Journal of sound and vibration, 308 (3–5), 431-440, 2007.

[3] Maugan F., Rigaud E., Perret-Liaudet J. Modelling of the nonlinear dynamic and vibroacoustic behaviour of a roots vacuum pump with gear backlash. International Gear Conference 2018, Lyon, France, 2018.

[4] Sakai T., Doi Y., Yamamoto K., Ogasawara T., Narita M. Theoretical and experimental analysis of rattling noise of automotive gearbox, SAE Technical Paper, 810773, 1-10, 1981.

[5] Singh R., Xie H., Comparin R. Analysis of automotive neutral gear rattle, Journal of Sound and Vibration, 131 (2), 177-196, 1989.

[6] Padmanabhan C., Singh R. Influence of clutch design on the reduction and perception of automotive transmission rattle noise, Noise-con 93, Williamsburg, VA, 1993.

[7] Wang M., Zhao W., Manoj R. Numerical modelling and analysis of automotive transmission rattle, Journal of Vibration and Control, 8 (7), 921-943, 2002.

[8] Chae C., Won K., Kang K. Measurement of transmission rattle sensitivity and calculation of driveline torsional vibration for gear rattle analysis, SAE Technical Paper, 2005-01-1785, 2005.

[9] Tangasawi O., Theodossiades S., Rahnejat H. Lightly loaded lubricated impacts: Idle gear rattle. Journal of Sound and Vibration. 308 (3–5), 418-430, 2007.

[10] Barthod M., Hayne B., Tébec J.-L., Pin J.-C. Experimental study of gear rattle excited by a multi-harmonic excitation. Applied Acoustics, 68 (9), 1003-1025, 2007.

[11] Bozca M. Torsional vibration model based optimization of gearbox geometric design parameters to reduce rattle noise in an automotive transmission. Mechanism and Machine Theory,45(11), 1583-1598, 2010.

[12] Kadmiri Y., Rigaud E., Perret-Liaudet J., Vary L. Experimental and numerical analysis of automotive rattle noise. Journal of Sound and Vibration 331(13), 3144-3157, 2012.

[13] Rust A., Brandl F., Thien G. Investigations into gear rattle phenomena – key parameters and their influence on gearbox noise, IMechE, C404/001, 113-120, 1990.

[14] Perret-Liaudet J., Rigaud E. Gear rattle noise – Noise-induced intermittency in a model of gear rattle. International Gear Conference, Lyon, France, 841-847, 2018.

[15] Karagiannis K., Pfeiffer F. Theoretical and experimental investigations of gear-rattling, Nonlinear Dynamics, 2 (5), 367-387, 1991.

[16] Kadmiri, Y., Perret-Liaudet J., Rigaud E., Le Bot A. Influence of multi-harmonics excitation on rattle noise in automotive gearboxes. Advances in Acoustics and Vibration, Vol 2011, ID 659797, 2011.

[17] Kunert A., Pfeiffer F. Stochastic Model for Rattling in Gear-Boxes. Nonlinear Dynamics in Engineering Systems, IUTAM Symposium, Stuttgart, Germany, 173-180, 1989.

[18] Perret-Liaudet J.; Rigaud E. Some effects of gear eccentricities on automotive rattle noise. Proceedings of the 10th international ASME power transmission and gearing conference, Paper 34794, 561-568, Las Vegas (USA), 2007.

[19] Ottewill J., Neild S., Wilson R. Intermittent gear rattle due to interactions between forcing and manufacturing errors. Journal of Sound and Vibration, 321 (3–5), 913-935, 2009.

[20] Ottewill J., Neild S., Wilson R. An investigation into the effect of tooth profile errors on gear rattle. Journal of Sound and Vibration, 329 (17), 3495-3506, 2010.

[21] Le Rouzic J., Le Bot A., Perret-Liaudet J., Guibert M., Rusanov A., Douminge L., Bretagnol F., Mazuyer D. Friction-induced vibration by Stribeck's Law: Application to wiper blade squeal noise. Tribology Letters, 49(3), 563–572, 2013.

[22] Welbourn D., Fundamental Knowledge of Gear Noise – a Survey. IMechE paper C117/79, 9-14, London, England, 1979.

[23] Souilliart T., Rigaud E., Le Bot A., Phalippou C. An energy approach for impact wear in water environment. Wear, 376-377, 738-746, 2017.

[24] Nagurka M., Huang S. A mass-spring-damper model of a bouncing ball. International Journal of Engineering Education, 22(2), 393-401, 2006.

[25] Carbonelli, A., Perret-Liaudet J., Rigaud E., Feki, M. Investigation of restitution coefficient and spring damper models for the bouncing ball problem. 8th International Conference on Multibody Systems, Nonlinear Dynamics, and Control, IDETC/CIE 2011, Washington, 93-501, 2011.

[26] Rigaud E., Sabot, J., Perret-Liaudet J.; Comprehensive approach for the vibrational response analysis of a gearbox (Approche globale pour l'analyse de la réponse vibratoire d'une transmission par engrenages). Revue Européenne des Eléments Finis. 9(1-2-3), 315-330, 2001.

[27] Carbonelli A., Rigaud E., Perret-Liaudet J. Vibro-Acoustic Analysis of Geared Systems—Predicting and Controlling the Whining Noise. Automotive NVH Technology, 63-79, Editors Fuchs A., Nijman E., Priebsch H-H., SpringerBriefs in Applied Sciences and Technology, Springer International Publishing. ISBN 978-3-319-24055-8, 2016.